Madeline Hille

The orographic influence on storm variability, extreme rainfall characteristics and rainfall-triggered landsliding in the central Nepalese Himalaya

submitted in partial fulfillment of the requirements for the degree of
Master of Science in Earth and Environmental Sciences
Department of Earth and Environmental Sciences The
University of Michigan

Accepted by:

Signature	Marin K. Clark Name	07/13/21 Date
Signature	Julia Cole Name	07/16/2021 Date
Department Chair Signature	Jeroen Ritsema Name	08/04/2021 Date

Earth and Environmental Sciences
UNIVERSITY OF MICHIGAN

LSA EARTH AND ENVIRONMENTAL SCIENCES
UNIVERSITY OF MICHIGAN

The orographic influence on storm variability, extreme rainfall characteristics and rainfall-triggered landsliding in the central Nepalese Himalaya

By
Madeline M. Hille

A thesis submitted in partial fulfillment
Of the requirements for the degree of
Master in Science
(Earth and Environmental Science)
In the University of Michigan
2021

Master's Committee:
Professor Marin K. Clark, *Advisor*
Professor Julia Cole, *Faculty Reader*
Professor Jeroen Ritsema, *Department Chair*

Acknowledgements

Completing the work presented in my thesis would not have been possible without the unending support and creative mentorship of my advisor, Marin Clark, nor without the teaching, guiding and valuable discussion from collaborators Drew Gronewold, Josh West and Dimitrios Zekkos. I want to thank my peers, Kirk Townsend and William Medwedeff, for being my steady mentors and friends, as well as Nikolas Midttun, Christine Nims, Abra Atwood and many other graduate students for fruitful discussion of geology, bike trips and countless laughs. Thank you to my reading committee, Marin Clark, Julie Cole and Jeroen Ritsema, for reviewing my thesis and providing constructive feedback. A special thank you to my parents, Carrie Van Buren and Joel Hille, and other loved ones for their unconditional support, understanding and open ears. Funding for this thesis was provided by individual and collaborative grants, including the National Science Foundation Collaborative Research award #1640797 to Clark, Zekkos and West, NSF grant #1640894 to West, the National Aeronautics and Space Administration (NASA) under grant No. 18-DISASTER18-0022, the Polar Geospatial Center NSF-OPP awards1043681 and 1559691 for access to Digital Globe satellite data ((National Geospatial Intelligence Agency) through a cooperative agreement with NSF (NextView License), and the Scott Turner Award in Earth and Environmental Sciences. And finally, I would like to thank Nepali collaborators Deepak Chamlagain, Sabin Tiwari and Suman Budhathoki, the Nepal Department of Hydrology and Meteorology and the International Centre for Mountain Development for access to rain gauge datasets that made this research possible.

Table of Contents

List of Tables

List of Figures

Abstract

Variation in extreme rainfall under the influence of orography plays an important yet poorly understood role in the erosion of mountains. In the steep terrain of the Himalaya, intense precipitation frequently triggers soil and shallow bedrock landslides during the summer monsoon. Characterizing monsoon-triggered landsliding as a dominant erosion process and hazard requires an understanding of the intensity and duration of precipitation during storms, but the daily resolution and sparse spatial coverage of local precipitation instrumental records are insufficient. Here we use NASA's Global Precipitation Measurement (GPM) IMERG 30-minute, 0.1x0.1 degree product scaled to match local rain gauge records to characterize extreme rainfall events (EREs) over a study area in central Nepal. We separate extreme events in the time series with a minimum dry period between storm arrivals and cluster them using a K-means multivariate approach. Results show variability in the intensity and duration of EREs with distance from the Himalayan range front in a pattern consistent with the orographic effect also observed on total precipitation volume. Storms of highest intensity and shortest duration are coincident with increased density in monsoon-driven landsliding.

1. Introduction

Orographic rainfall contributes to focused, intense erosion in mid-latitude ranges: shaping the relief of mountain ranges and increasing the potential for frequent landsliding. Moist air parcels saturate when encountering high topography, leading to concentrated precipitation on the lower slopes of steep mountain fronts and a semi-arid rain shadow at higher elevations that tends to persist over diurnal and seasonal cycles (Houze, 2012; Roe, 2005). Across some orogens, mean annual precipitation reflects a strong orographic effect (Bookhagen & Burbank, 2006) that is closely coupled with spatial patterns in relief and erosion rates (Roe et al., 2003). Shallow landsliding and debris flows dominate the hillslope erosional process on steep and threshold hillslopes, often in response to individual prolonged or intense storm events generated by orography (Burbank et al., 2012; Gabet, Pratt-Sitaula, et al., 2004).

It is commonly accepted that higher volumes of rain result in greater frequencies or sizes of landslides (Sidle Hirotaka Ochiai et al., 2006), and that seasonal precipitation accumulation saturates hillslopes and drives landsliding (Gabet, Pratt-Sitaula, et al., 2004). But the variability of rainfall at minute to hourly scales also influences where and when landslides occur (Iverson, 2000; Montgomery & Dietrich, 1994; Rosso et al., 2006). Shallow landslides are triggered by high pore pressures following topographically controlled groundwater flow and infiltration over minutes to hours to weeks (Iverson, 2000), and are thus modulated by the interplay between hydrologic properties of the subsurface (Bellugi et al., 2015) and the style and variability of precipitation. Local thresholds of rainfall intensity and duration linked to landsliding are commonly derived where detailed data exist (Dahal & Hasegawa, 2008). However, records that connect storm characteristics (including intensity and duration of rainfall) to the size and location of landsliding are scarce (Bellugi et al., 2015). This limits our understanding of how rainfall variability over short timescales influences landsliding, particularly in orographic settings with seasonal precipitation and steep climatic and topographic gradients (Gabet, Pratt-Sitaula, et al., 2004; Gariano & Guzzetti, 2016)

Precipitation over steep terrain is notoriously complex because of micro-scale physics and location-specific airflow (Roe, 2005). Short and intense storm events are particularly difficult to model because the processes that govern them are often non-stationary and stochastic (Fatichi et al., 2016; Terzago et al., 2018). High precipitation accumulation is a hallmark of

orographic rainfall, yet some studies have shown that orography may depress rainfall intensity in short duration storms (< 1 hr) (Allamano et al., 2009; Avanzi et al., 2015; Marra et al., 2021; Zhang et al., 2014) and enhance intensity in storms of longer duration (1-6 hrs) (Marra et al., 2021). Disentangling orographically influenced storm variability poses a significant challenge in part because precipitation datasets often lack the spatial and temporal resolution to resolve convective-scale, short-duration storm events. Satellite-derived precipitation are inaccurate over high relief and altitude (Andermann et al., 2011; Bharti et al., 2016; Mei et al., 2014) and networks of rain gauges in areas of such difficult access are sparsely populated. Recent advances in satellite precipitation monitoring with high temporal resolution and continuous spatial coverage (e.g., TRMM, CHIRPS and IMERG; (Funk et al., 2015; Huffman et al., 2019)) offer the opportunity to expand insight into the relationship between orography and rainfall characteristics. The availability of repeat, high-resolution (sub-meter) optical imagery facilitates the derivation of annual spatial patterns of landsliding in otherwise inaccessible terrain (Marc et al., 2015), which, when compared to statistical interpretations of high temporal resolution precipitation patterns, may help us understand how precipitation, orography and erosion processes interact.

The uniquely extreme environment of the central Nepalese Himalaya allows us to study the critical effects of orography on variable storm precipitation and the annual erosion cycle. Steep hillslopes are vulnerable to intense rain during the summer monsoon and experience frequent shallow landslides and debris flows that damage rural communities and kill hundreds of people each year (Petley et al., 2007). The prominent relief of the Himalaya is known to have a long-term orographic effect on mean annual precipitation of up to 4 m/yr over the range front (Anders et al., 2006; Bookhagen & Burbank, 2006, 2010; Roe, 2005) that can be strongly influenced by relief at local scales (Barros et al., 2006). Here, we look in greater detail at the characteristics (e.g., intensity and duration) of extreme storms during the summer monsoon to explore the influence of orography and their spatial correlation with annual landsliding.

In this study, we calibrate GPM IMERG-V06 data with the daily record from local Nepal Department of Hydrology and Meteorology (DHM) rain gauges to produce high-temporal resolution records of precipitation at point locations. We delineate independent storms using location-specific minimum dry periods, define extreme storms over a certain intensity threshold, and quantify variability and spatial patterns in storm characteristics using paired K-means

agglomerative cluster and principal component analyses. Storm variability is compared to mapped inventories of monsoon-triggered landslides from 2010-2014 to evaluate the influence of orographic precipitation on spatial patterns in erosion.

2. Methods

2.1 Study area

The central Nepalese Himalaya is a collisional tectonic setting with coupled gradients in topography, precipitation, and erosion (Hodges et al., 2001) (Figure 1). The "physiographic transition" refers to an abrupt increase in elevation, steeper slopes and greater relief at mid-altitudes in the range (Hodges et al., 2001; Wobus et al., 2003, 2006), which enhances the orographic barrier of the Himalaya and concentrates rainfall (Bookhagen & Burbank, 2006; Gabet, Pratt-Sitaula, et al., 2004). We have targeted the Melamchi Khola, a tributary catchment to the Indrawati River, for study (Figure 1). The Melamchi is oriented perpendicular to the physiographic transition and located entirely within the Greater Himalayan Sequence of migmatites and gneisses (Dhital, 2015; Figure S1), allowing us to evaluate landsliding across a steep gradient in topography and precipitation while minimizing the dependence of landslide susceptibility on lithology.

2.2 Data sources

We use two primary precipitation datasets in this study: (1) local rain gauges operated by the Nepal Department of Hydrology and Meteorology (DHM) and the International Centre for Integrated MOuntain Development (Shea et al., 2015), and (2) NASA's Global Precipitation Mission (GPM) Integrated Multi-satellitE Retrievals for GPM (IMERG) satellite-based dataset (Huffman et al., 2019) (Figure 1). The current network of local rain gauges measures daily precipitation and an orographic effect on monsoon rainfall reflected in the long-term TRMM record (Figure 1B). However, the network lacks the subdaily temporal resolution needed to characterize storm events. NASA's gridded 0.1x0.1-degree IMERG product provides global precipitation estimates every 30-minutes in mm/hr from merged and intercalibrated microwave

precipitation and infrared estimates and is spatially continuous. IMERG rainfall depth is underestimated across steep terrain relative to ground-based data and is therefore insufficient as a standalone dataset for this study (Lee et al., 2019; Xu et al., 2017); Figure 1).

Satellite-derived products like IMERG have previously been shown to perform poorly over mountainous regions with high relief (Andermann et al., 2011; Barros et al., 2006; Mei et al., 2016), particularly in the case of short-duration (Mei et al., 2014) and heavy rainfall events (Bharti et al., 2016; Y. C. Gao & Liu, 2013; Moazami & Najafi, 2021; Tan et al., 2016). Although satellite-derived products do reasonably well at estimating the occurrence of rainfall relative to ground-based data over complex topography (Dinku et al., 2008; Nepal et al., 2021; Tan et al., 2016), timing estimates of peak rainfall during a storm can also be significantly different from gauge estimates, depending on the magnitude and duration of the event (Hossain et al., 2004). It is also likely that the DHM network underestimates rainfall due to wind-dependent under-catch (Pollock et al., 2018; Rodda & Dixon, 2012). In Nepal, studies comparing IMERG and gauge data show a consistent underestimation of mean annual rainfall by IMERG relative to available DHM gauge data (Nepal et al., 2021; Sharma, Chen, et al., 2020; Sharma, Khadka, et al., 2020). The discrepancy between the IMERG and ground-based measurements of very short duration (<30 minutes) and extreme convective-scale storm events may be explained by the 30-minute temporal resolution limited by the overpass frequency of passive microwave sensors (Mei et al., 2014), or by the infrared sensors that effectively see cloud tops but weakly estimate the intensity or volume of surface precipitation (Sapiano & Arkin, 2009; Tan et al., 2016).

2.3 Merging precipitation datasets

In this study, we calibrate the IMERG data with the DHM rain gauge dataset to produce a rainfall product with 30-minute rainfall intensity. We scale the summed IMERG 30-minute grid cell precipitation at each gauge to match daily rainfall records such that total daily GPM rainfall is equal to total gauge daily rainfall (Figure 2). We supplement the IMERG record with the Tropical Rainfall Measuring Mission (TRMM) 3B42V6 data collected prior to the 2014 inception of the IMERG catalog. The resulting precipitation dataset is a point-location timeseries with 30-minute rainfall intensity measurements in mm/hr spanning the monsoon season (June 01-September 30) over the period 2010-2018.

2.4 Defining storms and extreme rainfall events (EREs)

Rainfall-induced landsliding is driven by excess pore fluid pressures during periods of intense rainfall. To characterize storms in precipitation timeseries, we first extract individual storms from the time series using a minimum dry period between measurable rainfall (Driscoll, 1989; Dunkerley, 2008; Gaál et al., 2014; Schleiss & Smith, 2016). We calculate the average inter-accumulation time (IAT) (Schleiss, 2017; Schleiss & Smith, 2016) for each rain gauge record for each monsoon year as the minimum dry period between definitive storm events (also referred to as the Minimum Interevent Time (MIT); (Gaál et al., 2014)). **Eq. 1** defines the IAT as the mean number of hours over which an arbitrary amount of rain accumulates (Δr) during the monsoon season (here, we use Δr = 2 mm).

$$IAT_{\Delta r} = \Delta r \frac{Time_{monsoon\ total\ hrs}}{Rainfall_{monsoon\ total\ mm}} \quad \textbf{Eq. 1}$$

The average IAT at each gauge ranges from ~1.5 to 8 hours across our study area (Table S1). Using the IAT method as a proxy for the MIT is preferable to applying a consistent dry period threshold at every station (such as a 6-hr MIT) because it allows for the duration and intensity of individual storm events to vary with respect to total rainfall and normalizes for the regional precipitation gradient (Schleiss & Smith, 2016). In this manner, we avoid artificially depressing the average intensity of storms in locations with greater monsoon rainfall totals and shorter dry periods between events, and vice versa.

Sample sizes of 20-120 individual storm events were determined for each of 46 rain gauges for each monsoon year. Storms are characterized by several properties hypothesized to influence erosion and landslide occurrence: duration (hrs), depth (mm), average intensity (mm/hr), peak intensity (mm/hr), and rainfall prior to the storm peak (mm) (Figure 2). A lognormal PDF is fit to the average intensity distribution of all storm events at each station and for each monsoon year. Any storm with an average intensity that falls above the 90th percentile is considered an ERE (Bookhagen & Burbank, 2010; Krishnamurthy et al., 2009; Malik et al., 2012); Appendix B and Figure S5).

2.5 Cluster analysis of extreme rainfall events (EREs)

To evaluate the spatial variability of storm characteristics relative to orography, we partitioned the bulk 2010-2018 ERE dataset into clusters using a K-means clustering technique. The K-means approach is an agglomerative method that partitions clusters based on similarity defined by the Euclidean distance metric. The K-means method also requires a pre-specified number of clusters for which we use the Elbow Method (Figure S6). Individual EREs are assigned to one of 10 clusters based on the five prescribed storm characteristics: duration, depth, average intensity, peak intensity, and rainfall prior to the storm peak. We then assign each gauge station to a cluster based on the cluster group for which a majority of the EREs are assigned. This results in a spatial distribution of cluster values based on the dominant storm characteristics observed at each gauge station. The spatial distribution does not change significantly by using fewer than 10 clusters in this approach, or with multiple clustering iterations (Appendix C).

We assess the interdependent relationships between ERE characteristics using a principal components analysis (PCA) based on the correlation matrix of the ERE dataset. Many of the storm properties that we have chosen to include in this analysis covary, and we use PCA here as a dimension-visualization tool in conjunction with our cluster analysis to determine how clusters differ over space in terms of their ERE characteristics. As a final step, we compare our cluster and PCA results with a catalog of monsoon-driven landslides from 2010-2014 in the Melamchi Valley (see Appendix C) to relate storm characteristics to monsoon-triggered landsliding. We limit the landslide catalog to 2010-2014 prior to the 2015 Mw7.8 Gorkha earthquake to avoid including a legacy earthquake effect on monsoon-driven landsliding.

3. Results

ERE intensity in Central Nepal varies with orography and follows the trend of mean monsoon rainfall intensity. Here we identify a spatial pattern of EREs over our study area using an interpolation spline-fit to the threshold ERE intensities between 2010-2018 at each rain gauge (Figure 3). Overall, EREs range from a threshold intensity of ~4 mm/hr over the Kathmandu basin to a maximum of ~20 mm/hr in the northern Melamchi Valley, which mirrors the sharp increase in mean monsoon rainfall intensities observed in the rain gauge dataset. Further north,

ERE intensity decreases and ranges from 4-13 mm/hr; however, the density of rain gauges and the availability of ground-based precipitation data in these northern areas is limited and intensities may be underestimated through gauge under-catching due to wind and snowfall (Kirkham et al., 2019). The yearly variation in the ERE thresholds is small to the south of the Melamchi Valley, and large north of the physiographic transition at ~47 km distance along our transect. At several gauge locations within the northern Melamchi, the ERE threshold fluctuates within a range of 10 mm/hr year-to-year (Figure 3; Figure S8). Importantly, the threshold ERE intensities put only a lower bound on the expected intensities of extreme events over Central Nepal; many EREs between 2010-2018 have average intensities that far exceed these thresholds by up to 110 mm/hr and experience peak intensities of >100 mm/hr (Figure S9).

We identify 5,261 storms that exceed the ERE threshold during the period of 2010-2018. The primary ERE clusters at each rain gauge are spatially distributed into two groups (A and B) (Figure 3). Principal components analysis (PCA) derives linear combinations of the five storm characteristics for which we ascertain differences between the storms typical of clusters A and B (Figure 4A). Both average storm intensity and peak storm intensity are negatively correlated with duration, prior rainfall and storm depth. This suggests that overall, EREs are typically short and intense or prolonged and less intense. Prolonged (>6 hours) EREs with a high 30-minute peak intensity are rare. The PCA shows that two components explain more than 88% of the variance in the ERE dataset, where components 1 and 2 are primarily composed of average and peak storm intensities and storm duration, depth, and prior rain, respectively. Variability in monsoon storm events is adequately described by these two groupings of strongly correlated storm properties. Details on the PCA including variable loadings and the proportion of variance explained by each component are listed in Table S2.

Clusters A and B are distinct in terms of the types of storms that occur in each. Cluster A includes storms with high intensities (both average and peak 30-minute intensities), whereas cluster B includes prolonged events with greater total rainfall and rainfall prior to the storm peak (Figure 4). Interestingly, the short duration storms (30 min to 3 hrs) that do occur over the space of cluster B experience average storm intensities equal to or greater than the intensities of storms in cluster A. Storms greater than ~3 hours in length are more intense in cluster A and less intense in cluster B. We observe no correlation with timing throughout the monsoon season; EREs in

both clusters occur stochastically and frequently (Figure S10). Importantly, clusters A and B also show a spatial pattern in ERE characteristics. Cluster A includes rain gauge stations that are situated between the physiographic transition and the highest peaks of the Central Nepalese Himalaya, focusing the shortest and most intense storms in the northern Melamchi Valley (Figure 3). The longer duration, less intense storms of Cluster B are recorded at stations located to the north of the Melamchi Valley and in the southern Melamchi south of the physiographic transition.

The loci of monsoon-driven landsliding in the Melamchi Valley occurs ~50-62 km from the range front, which spatially correlates with both the highest peak in ERE intensity thresholds and the short and intense storms of cluster A (Figure 3). Landslide density is agglomerated for monsoon years 2010-2014 to avoid the potential legacy effects of the 2015 Mw7.8 Gorkha event. In the five-year period of analysis, over 600 shallow landslides occurred during the monsoons, with most occurring in the northern Melamchi Valley where slopes are steepest and intense precipitation is frequent. Specific intensity-duration thresholds for shallow landsliding in central Nepal are scarce because sub-daily resolution precipitation data and mapped monsoon-driven landslide inventories with specific trigger times are unavailable. Dahal and Hasegawa (2008) determined an intensity-duration threshold for monsoon-driven landsliding that is limited to intense rainfall lasting > 5 hours; this Himalaya-specific threshold requires greater rainfall intensities than the global rainfall-triggered landslide threshold from Guzzetti et al., 2008 (Figure 4). Most EREs that we identify between the monsoon years 2010-2018 are of shorter duration than 5 hrs and very few storms fall above the Himalaya-specific threshold (Dahal & Hasegawa, 2008) even when extrapolated out to storm events lasting < 5 hours. However, the peak intensities of many of the EREs fall above the Himalaya landslide threshold, with the majority being storm events of shorter duration in cluster A (Figure S9).

4. Discussion

The separation of individual storms offers a holistic perspective on the variability of landslide-triggering precipitation. Satellite-based observations calibrated with ground data capture a regional trend in storm characteristics. Short, frequent, and high intensity events are concentrated over the forefront of the Himalayan range north of the physiographic transition

where topography and slope gradients are steepest (Figure 3). While Bookhagen & Burbank (2010) show that orography focuses high seasonal precipitation totals near the physiographic transition, we show that Himalayan orography also causes precipitation to be distinctly more intense. The observation that orography enhances storm intensity is also consistent with observations from 1–6 hour long cyclones over steep topography in the southeast Mediterranean (Marra et al., 2021).

At a finer scale, the relationship between intensity and topography varies as a function of total storm duration. We observe comparable average and peak ERE intensities between clusters A and B at short durations (< 1 hour), suggesting that these infrequent and extremely intense events are indiscriminate of topography. It is only at longer durations (> 1 hr) that EREs in cluster A are consistently of higher intensities compared to cluster B (Figure 4B). Within storms, peak 30-minute rainfall intensities are also similar between clusters at any storm duration, suggesting that low-intensity storm events in any location may include short bursts of comparably intense rainfall (Figure S8). The measurement interval of the satellite data (30 minutes) limits how much we can say about the patterns of rainfall with respect to orography at durations less than one hour. For example, the "reverse orographic effect" (intensities decrease with increasing elevation) seen in short duration periods (< 1 hr) elsewhere (Allamano et al., 2009; Avanzi et al., 2015; Marra et al., 2021; Zhang et al., 2014) cannot be evaluated with our dataset.

While we do not differentiate storms with respect to atmospheric dynamics (i.e., convective vs. stratiform conditions), the distribution of ERE intensities and durations suggests that our methodology identifies storms initiating from either process. We interpret the highest-intensity and short-duration (30-minute) storms occurring in both clusters A and B as convective cells originating from rising unstable air parcels and the super-cooling of water vapor (Roe, 2005). Orography has a poorly understood effect on extreme rainfall at short durations (Bongioannini Cerlini et al., 2005). Convective cells occur regardless of the presence of relief, although some studies show that convective rain is affected by airflow dynamics at the forefront of mountain ranges (Bongioannini Cerlini et al., 2005; Houze, 2012). Stratiform processes, on the other hand, enhance rainfall at higher elevations and perhaps at longer durations (Kirschbaum & Stanley, 2018). Valley-located gauges may receive more precipitation than neighboring ridges because such high relief results in lower water vapor content (Roe, 2005) although at small

scales rainfall can reach high elevations through the advection of cloud vapor (Barros et al., 2006). Two of the rain gauges in our dataset located near or on the Melamchi ridge (stations Tarke Ghyang and Sarmathang; Figure 1) consistently record frequent and high intensity events (Figure 3) but may be more prone to error from local airflow on ridges (Roe, 2005; Talchabhadel et al., 2017). Given the likelihood of under-catch, the minimum ERE intensities that we report for the northern Melamchi are likely underestimated and miss convective bursts of rainfall at higher intensities (>100 mm/hr), implying that more EREs may exceed landslide thresholds at short durations than are reported here.

We note no consistency in the timing of EREs with respect to the beginning or end of the monsoon season over the bulk of our study period (Figure S9), although it is possible that EREs occurring late in the monsoon season trigger landslides in near-saturated conditions after repeated monsoon precipitation has elevated the groundwater table (Dahal & Hasegawa, 2008; Gabet, Burbank, et al., 2004). This, coupled uncertain landslide event timing within the monsoon season, prevents us from correlating specific landslides to specific EREs and establishing a rainfall threshold for this study area. However, if we extrapolate published landslide thresholds for Nepal (Dahal & Hasegawa, 2008) to storm events <5 hours in length, fewer than ~20 storms over the 2010-2018 period qualify as landslide-triggering events (Figure 4B). We speculate that these less frequent, high-intensity EREs exhibited in cluster A trigger the majority of shallow landslides within the Melamchi Valley during each monsoon season.

While orographic rainfall is likely a primary landslide trigger, the complex interplay between tectonics, climate and erosion in this setting cannot be overlooked. Our results show that extreme rainfall is spatially coincident with monsoon-triggered landsliding: the area of densest landsliding in the Melamchi is closely coupled to the occurrence of intense EREs of durations < 10 hours. However, this narrow band of increased ERE intensity is also coincident with steep topography and exhumed, fractured bedrock, both of which make the hillslopes more susceptible to failure (Murray et al., 2018). While steeper slopes increase the driving forces to landsliding, the relationship between slope angle and rainfall-triggered landslide frequency is sometimes unclear on hillslopes >30 degrees (Coe et al., 2004; J. Gao & Maro, 2010; de Rose, 2013) and thinner soils on the steepest hillslopes may cause less frequent landsliding (Prancevic et al., 2020). While the tectonic and topographic contributions are not quantified here, we posit that

over the orographic focusing of extreme rainfall is likely to be the primary climatic boundary condition that modulates erosion in the Himalaya.

Conclusions

We present a novel approach to merging high-temporal resolution GPM IMERG data with local rain gauge records combined with a multidimensional approach to defining storm characteristics that relate to rainfall triggered landsliding. In the central Nepalese Himalaya, storm characteristics that influence landsliding (intensity, duration, depth, and prior rainfall) vary with respect to distance from the physiographic transition and mirror gradients in seasonal rainfall totals, topography, and erosion. Precipitation variability and intensity is strongly influenced by orography: frequent and intense storm events occur over steep hillslopes with high relief at mid-elevations range, while storm events are longer and less intense (mm/hr) over the lower foothills and near the headwaters. The association of shallow soil and bedrock landsliding frequency with storm characteristics suggests that frequent, intense storms concentrated at mid-elevations in the range are the primary climate drivers to hillslope erosion in the Himalaya.

References

Allamano, P., Claps, P., Laio, F., & Thea, C. (2009). A data-based assessment of the dependence of short-duration precipitation on elevation. *Physics and Chemistry of the Earth*, *34*(10–12), 635–641. https://doi.org/10.1016/j.pce.2009.01.001

Andermann, C., Bonnet, S., & Gloaguen, R. (2011). Evaluation of precipitation data sets along the Himalayan front. *Geochemistry, Geophysics, Geosystems*, *12*(7). https://doi.org/10.1029/2011GC003513

Anders, A. M., Roe, G. H., Hallet, B., Montgomery, D. R., Finnegan, N. J., & Putkonen, J. (2006). Spatial patterns of precipitation and topography in the Himalaya. *Special Paper of the Geological Society of America*, *398*, 39–53. https://doi.org/10.1130/2006.2398(03)

Avanzi, F., de Michele, C., Gabriele, S., Ghezzi, A., & Rosso, R. (2015). Orographic signature on extreme precipitation of short durations. *Journal of Hydrometeorology*, *16*(1), 278–294. https://doi.org/10.1175/JHM-D-14-0063.1

Barros, A. P., Chiao, S., Lang, T. J., Burbank, D., & Putkonen, J. (2006). From weather to climate-Seasonal and interannual variability of storms and implications for erosion processes in the From weather to climate-Seasonal and interannual variability of storms and implications for erosion processes in the Himalaya. https://doi.org/10.1130/2006.2398(02)

Bellugi, D., Milledge, D. G., Dietrich, W. E., Perron, J. T., & McKean, J. (2015). Predicting shallow landslide size and location across a natural landscape: Application of a spectral clustering search algorithm. *Journal of Geophysical Research F: Earth Surface*, *120*(12), 2552–2585. https://doi.org/10.1002/2015JF003520

Bharti, V., Singh, C., Ettema, J., & Turkington, T. A. R. (2016). Spatiotemporal characteristics of extreme rainfall events over the Northwest Himalaya using satellite data. *International Journal of Climatology*, *36*(12), 3949–3962. https://doi.org/10.1002/joc.4605

Bongioannini Cerlini, P., Emanuel, K. A., & Todini, E. (2005). Orographic effects on convective precipitation and space-time rainfall variability: preliminary results. *Hydrology and Earth System Sciences*, *9*(4). https://doi.org/10.5194/hess-9-285-2005

Bookhagen, B., & Burbank, D. W. (2006). Topography, relief, and TRMM-derived rainfall variations along the Himalaya. *Geophysical Research Letters*, *33*(8). https://doi.org/10.1029/2006GL026037

Bookhagen, B., & Burbank, D. W. (2010). Toward a complete Himalayan hydrological budget: Spatiotemporal distribution of snowmelt and rainfall and their impact on river discharge. *Journal of Geophysical Research: Earth Surface*, *115*(3). https://doi.org/10.1029/2009JF001426

Burbank, D. W., Bookhagen, B., Gabet, E. J., & Putkonen, J. (2012, November). Modern climate and erosion in the Himalaya. *Comptes Rendus - Geoscience*. https://doi.org/10.1016/j.crte.2012.10.010

Coe, J. A., Michael, J. A., Covelli, R. A., Savage, W. Z., Laprade, W. T., & Nashem, W. D. (2004). Probabilistic Assessment of Precipitation-Triggered Landslides Using Historical Records of Landslide Occurrence, Seattle, Washington. *Environmental and Engineering Geoscience*, *10*(2). https://doi.org/10.2113/10.2.103

Dahal, R. K., & Hasegawa, S. (2008). Representative rainfall thresholds for landslides in the Nepal Himalaya. *Geomorphology*, *100*(3–4), 429–443. https://doi.org/10.1016/j.geomorph.2008.01.014

Dinku, T., Chidzambwa, S., Ceccato, P., Connor, S. J., & Ropelewski, C. F. (2008). Validation of high-resolution satellite rainfall products over complex terrain. *International Journal of Remote Sensing*, *29*(14), 4097–4110. https://doi.org/10.1080/01431160701772526

Driscoll, E. D. , P. G. E. , S. E. W. , & S. P. E. (1989). Analysis of Storm Event Characteristics for Selected Rainfall Gages Through Out the United States.

Dunkerley, D. (2008, December 30). Identifying individual rain events from pluviograph records: A review with analysis of data from an Australian dryland site. *Hydrological Processes*. https://doi.org/10.1002/hyp.7122

Fatichi, S., Ivanov, V. Y., Paschalis, A., Peleg, N., Molnar, P., Rimkus, S., et al. (2016). Uncertainty partition challenges the predictability of vital details of climate change. *Earth's Future*, *4*(5), 240–251. https://doi.org/10.1002/2015EF000336

Funk, C., Peterson, P., Landsfeld, M., Pedreros, D., Verdin, J., Shukla, S., et al. (2015). The climate hazards infrared precipitation with stations - A new environmental record for monitoring extremes. *Scientific Data*, *2*. https://doi.org/10.1038/sdata.2015.66

Gaál, L., Molnar, P., & Szolgay, J. (2014). Selection of intense rainfall events based on intensity thresholds and lightning data in Switzerland. *Hydrology and Earth System Sciences*, *18*(5), 1561–1573. https://doi.org/10.5194/hess-18-1561-2014

Gabet, E. J., Pratt-Sitaula, B. A., & Burbank, D. W. (2004). Climatic controls on hillslope angle and relief in the Himalayas. *Geology*, *32*(7), 629–632. https://doi.org/10.1130/G20641.1

Gabet, E. J., Burbank, D. W., Putkonen, J. K., Pratt-Sitaula, B. A., & Ojha, T. (2004). Rainfall thresholds for landsliding in the Himalayas of Nepal. *Geomorphology*, *63*(3–4), 131–143. https://doi.org/10.1016/j.geomorph.2004.03.011

Gao, J., & Maro, J. (2010). Topographic controls on evolution of shallow landslides in pastoral Wairarapa, New Zealand, 1979-2003. *Geomorphology*, *114*(3), 373–381. https://doi.org/10.1016/j.geomorph.2009.08.002

Gao, Y. C., & Liu, M. F. (2013). Evaluation of high-resolution satellite precipitation products using rain gauge observations over the Tibetan Plateau. *Hydrology and Earth System Sciences*, *17*(2), 837–849. https://doi.org/10.5194/hess-17-837-2013

Gariano, S. L., & Guzzetti, F. (2016, November 1). Landslides in a changing climate. *Earth-Science Reviews*. Elsevier B.V. https://doi.org/10.1016/j.earscirev.2016.08.011

Guzzetti, F., Peruccacci, S., Rossi, M., & Stark, C. P. (2008). The rainfall intensity-duration control of shallow landslides and debris flows: An update. *Landslides*, *5*(1), 3–17. https://doi.org/10.1007/s10346-007-0112-1

Hodges, K. v., Hurtado, J. M., & Whipple, K. X. (2001). Southward extrusion of Tibetan crust and its effect on Himalayan tectonics. *Tectonics*, *20*(6), 799–809. https://doi.org/10.1029/2001TC001281

Hossain, F., Anagnostou, E. N., Dinku, T., & Borga, M. (2004). Hydrological model sensitivity to parameter and radar rainfall estimation uncertainty. *Hydrological Processes*, *18*(17), 3277–3291. https://doi.org/10.1002/hyp.5659

Houze, R. A. (2012). Orographic effects on precipitating clouds. *Reviews of Geophysics*, *50*(1). https://doi.org/10.1029/2011RG000365

Huffman, G. J., Bolvin, D. T., Nelkin, E. J., & Tan, J. (2019). *Integrated Multi-satellitE Retrievals for GPM (IMERG) Technical Documentation*.

Iverson, R. M. (2000). Landslide triggering by rain infiltration. *Water Resources Research*, *36*(7), 1897–1910. https://doi.org/10.1029/2000WR900090

Kirkham, J. D., Koch, I., Saloranta, T. M., Litt, M., Stigter, E. E., Møen, K., et al. (2019). Near real-time measurement of snow water equivalent in the Nepal Himalayas. *Frontiers in Earth Science*, *7*. https://doi.org/10.3389/feart.2019.00177

Kirschbaum, D., & Stanley, T. (2018). Satellite-Based Assessment of Rainfall-Triggered Landslide Hazard for Situational Awareness. *Earth's Future*, *6*(3), 505–523. https://doi.org/10.1002/2017EF000715

Krishnamurthy, C. K. B., Lall, U., & Kwon, H.-H. (2009). Changing Frequency and Intensity of Rainfall Extremes over India from 1951 to 2003. *Journal of Climate*, *22*(18). https://doi.org/10.1175/2009JCLI2896.1

Lee, J., Lee, E. H., & Seol, K. H. (2019). Validation of Integrated MultisatellitE Retrievals for GPM (IMERG) by using gauge-based analysis products of daily precipitation over East Asia. *Theoretical and Applied Climatology*, *137*(3–4), 2497–2512. https://doi.org/10.1007/s00704-018-2749-1

Malik, N., Bookhagen, B., Marwan, N., & Kurths, J. (2012). Analysis of spatial and temporal extreme monsoonal rainfall over South Asia using complex networks. *Climate Dynamics*, *39*(3), 971–987. https://doi.org/10.1007/s00382-011-1156-4

Marc, O., Hovius, N., Meunier, P., Uchida, T., & Hayashi, S. (2015). Transient changes of landslide rates after earthquakes. *Geology*, *43*(10), 883–886. https://doi.org/10.1130/G36961.1

Marra, F., Armon, M., Borga, M., & Morin, E. (2021). Orographic Effect on Extreme Precipitation Statistics Peaks at Hourly Time Scales. *Geophysical Research Letters*, *48*(5). https://doi.org/10.1029/2020GL091498

Mei, Y., Anagnostou, E. N., Nikolopoulos, E. I., & Borga, M. (2014). Error analysis of satellite precipitation products in mountainous basins. *Journal of Hydrometeorology*, *15*(5), 1778–1793. https://doi.org/10.1175/JHM-D-13-0194.1

Mei, Y., Nikolopoulos, E. I., Anagnostou, E. N., Zoccatelli, D., & Borga, M. (2016). Error analysis of satellite precipitation-driven modeling of flood events in complex alpine terrain. *Remote Sensing*, *8*(4). https://doi.org/10.3390/rs8040293

Moazami, S., & Najafi, M. R. (2021). A comprehensive evaluation of GPM-IMERG V06 and MRMS with hourly ground-based precipitation observations across Canada. *Journal of Hydrology*, *594*. https://doi.org/10.1016/j.jhydrol.2020.125929

Montgomery, D. R., & Dietrich, W. E. (1994). *A physically based model for the topographic control on shallow landsliding*. *WATER RESOURCES RESEARCH* (Vol. 30).

Murray, K., Clark, M., Niemi, N., Quackenbush, P., West, A. J., Medwedeff, W., & Chamlagain, D. (2018). Focused Pulse of Rapid Erosion in Central Nepal Related to Himalayan Fault Motion. In *American Geophysical Union, Fall Meeting 2018*. Retrieved from https://ui.adsabs.harvard.edu/abs/2018AGUFMEP53A..04M

Nepal, B., Shrestha, D., Sharma, S., Singh Shrestha, M., Aryal, D., & Shrestha, N. (2021). Assessment of GPM-Era Satellite Products' (IMERG and GSMaP) Ability to Detect Precipitation Extremes over Mountainous Country Nepal. https://doi.org/10.3390/atmos

Petley, D. N., Hearn, G. J., Hart, A., Rosser, N. J., Dunning, S. A., Oven, K., & Mitchell, W. A. (2007). Trends in landslide occurrence in Nepal. *Natural Hazards*, *43*(1), 23–44. https://doi.org/10.1007/s11069-006-9100-3

Pollock, M. D., O'Donnell, G., Quinn, P., Dutton, M., Black, A., Wilkinson, M. E., et al. (2018). Quantifying and Mitigating Wind-Induced Undercatch in Rainfall Measurements. *Water Resources Research*, *54*(6), 3863–3875. https://doi.org/10.1029/2017WR022421

Prancevic, J. P., Lamb, M. P., McArdell, B. W., Rickli, C., & Kirchner, J. W. (2020). Decreasing Landslide Erosion on Steeper Slopes in Soil-Mantled Landscapes. *Geophysical Research Letters*, *47*(10). https://doi.org/10.1029/2020GL087505

Rodda, J. C., & Dixon, H. (2012). Rainfall measurement revisited. *Weather*, *67*(5), 128–131. https://doi.org/10.1002/wea.875

Roe, G. H. (2005). *OROGRAPHIC PRECIPITATION*. *Annual Review of Earth and Planetary Sciences*.

Roe, G. H., Montgomery, D. R., & Hallet, B. (2003). Orographic precipitation and the relief of mountain ranges. *Journal of Geophysical Research: Solid Earth*, *108*(B6). https://doi.org/10.1029/2001jb001521

de Rose, R. C. (2013). Slope control on the frequency distribution of shallow landslides and associated soil properties, North Island, New Zealand. *Earth Surface Processes and Landforms*, *38*(4), 356–371. https://doi.org/10.1002/esp.3283

Rosso, R., Rulli, M. C., & Vannucchi, G. (2006). A physically based model for the hydrologic control on shallow landsliding. *Water Resources Research*, *42*(6). https://doi.org/10.1029/2005WR004369

Sapiano, M. R. P., & Arkin, P. A. (2009). An intercomparison and validation of high-resolution satellite precipitation estimates with 3-hourly gauge data. *Journal of Hydrometeorology*, *10*(1), 149–166. https://doi.org/10.1175/2008JHM1052.1

Schleiss, M. (2017). Scaling and distributional properties of precipitation interamount times. *Journal of Hydrometeorology*, *18*(4), 1167–1184. https://doi.org/10.1175/JHM-D-16-0221.1

Schleiss, M., & Smith, J. A. (2016). Two simple metrics for quantifying rainfall intermittency: The burstiness and memory of interamount times. *Journal of Hydrometeorology*, *17*(1), 421–436. https://doi.org/10.1175/JHM-D-15-0078.1

Sharma, S., Chen, Y., Zhou, X., Yang, K., Li, X., Niu, X., et al. (2020). Evaluation of GPM-Era satellite precipitation products on the southern slopes of the central Himalayas against rain gauge data. *Remote Sensing*, *12*(11). https://doi.org/10.3390/rs12111836

Sharma, S., Khadka, N., Hamal, K., Shrestha, D., Talchabhadel, R., & Chen, Y. (2020). How Accurately Can Satellite Products (TMPA and IMERG) Detect Precipitation Patterns, Extremities, and Drought Across the Nepalese Himalaya? *Earth and Space Science*, *7*(8). https://doi.org/10.1029/2020EA001315

Shea, J. M., Wagnon, P., Immerzeel, W. W., Biron, R., Brun, F., & Pellicciotti, F. (2015, April 3). A comparative high-altitude meteorological analysis from three catchments in the Nepalese Himalaya. https://doi.org/10.1080/07900627.2015.1020417

Sidle Hirotaka Ochiai, R. C., Bougeret, J.-L., Bebout, G. E., Fesen, C. G., Friedrichs, C. T., Haese, R. R., et al. (2006). LANDSLIDES Processes, Prediction, and Land Use Library of Congress Cataloging-in-PubJication Data.

Talchabhadel, R., Karki, R., & Parajuli, B. (2017). Intercomparison of precipitation measured between automatic and manual precipitation gauge in Nepal. *Measurement: Journal of the International Measurement Confederation*, *106*, 264–273. https://doi.org/10.1016/j.measurement.2016.06.047

Tan, J., Petersen, W. A., & Tokay, A. (2016). A Novel Approach to Identify Sources of Errors in IMERG for GPM Ground Validation. https://doi.org/DOI: 10.1175/JHM-D-16-0079.1

Terzago, S., Palazzi, E., & von Hardenberg, J. (2018). Stochastic downscaling of precipitation in complex orography: A simple method to reproduce a realistic fine-scale climatology.

Natural Hazards and Earth System Sciences, *18*(11), 2825–2840. https://doi.org/10.5194/nhess-18-2825-2018

Wobus, C. W., Hodges, K. v, & Whipple, K. X. (2003). *Has focused denudation sustained active thrusting at the Himalayan topographic front? Geology*. Retrieved from https://pubs.geoscienceworld.org/gsa/geology/article-pdf/31/10/861/3524253/i0091-7613-31-10-861.pdf

Wobus, C. W., Whipple, K. X., & Hodges, K. v. (2006). Neotectonics of the central Nepalese Himalaya: Constraints from geomorphology, detrital40Ar/39Ar thermochronology, and thermal modeling. *Tectonics*, *25*(4). https://doi.org/10.1029/2005TC001935

Xu, R., Tian, F., Yang, L., Hu, H., Lu, H., & Hou, A. (2017). Ground validation of GPM IMERG and trmm 3B42V7 rainfall products over Southern Tibetan plateau based on a high-density rain gauge network. *Journal of Geophysical Research*, *122*(2), 910–924. https://doi.org/10.1002/2016JD025418

Zhang, K., Pan, S., Cao, L., Wang, Y., Zhao, Y., & Zhang, W. (2014). Spatial distribution and temporal trends in precipitation extremes over the Hengduan Mountains region, China, from 1961 to 2012. *Quaternary International*, *349*, 346–356. https://doi.org/10.1016/j.quaint.2014.04.050

Appendix References

Chen, Y., Ebert, E. E., Walsh, K. J. E., & Davidson, N. E. (2013). Evaluation of TMPA 3B42 daily precipitation estimates of tropical cyclone rainfall over Australia. *Journal of Geophysical Research Atmospheres*, *118*(21), 11,966-11,978. https://doi.org/10.1002/2013JD020319

Legates and Liberty (1998) Precipitation measurement biases in the United States. *Water Resources Bulletin, 29(5),* 855-861.

Appendices

Appendix A. Details on data collection and error consideration

DHM rain gauge network details

The Nepal DHM rain gauge network employs a mix of over 300 automatic tipping bucket rain gauges and standard manual rain gauges (Talchabhadel et al., 2016; Dahal and Hasegawa, 2008). The DHM relies on part-time employees to read the standard gauges every day at 8:45 am (03 UTC) and report the daily total rainfall in mm via email to the DHM office in Kathmandu. DHM manual gauges are advertised as standard 8" gauges used by the U.S. National Weather Service, consisting of a measuring stick, overflow can, collector funnel and measuring tube (Talchabhadel et al., 2016). Rain infiltrates the collector funnel and fills the measuring tube; if rainfall is exceedingly heavy, the overflow falls into the surrounding can. It is unclear how overflow rain is measured or if it measured, which may lead to considerable error in daily rainfall measurements during the monsoon season when we see heavy rain. Part-time DHM employees otherwise use the measuring stick to read daily rainfall from the collection tube. Automatic tipping bucket gauges are notably rare within the DHM gauge network, and many of them are stationed at higher altitudes (Talchabhadel et al., 2016).

Each type of rain gauge assumes different sources of error. The World Meteorological Organization estimates a standard rain gauge error of 5% or 0.1 mm, whichever is greatest (Legates and Liberty, 1998). Gauges typically underestimate rainfall due to wind, evaporation, and the addition of water on the internal walls of the gauge when it is emptied. Strong winds associated with the summer monsoon likely contribute to underestimates during the monsoon season (Pollock et al., 2018; Rodda & Dixon, 2012), and topographic location has also been shown to influence rain gauge collection (Bookhagen and Burbank, 2006; Barros et al., 2006; Roe 2005). All sources of gauge error can result in both random and systematic errors in rainfall measurement (Y. Chen et al., 2013). Another source for error in either type of gauge is the possibility that employees might not be reading and reporting daily rainfall at exactly 8:45 am every day, which could result in discrepancies between the two types of gauges and either over or underestimates of daily rainfall (Talchabhadel et al., 2016).

Rain gauge precipitation data cleaning methods

For many of the reasons listed above, the DHM gauge time series are often discontinuous and show long periods of time without reported data, or suspiciously long periods of time where zero rain was falling during the intense summer monsoon. These periods are likely due to reporting errors or instrumentation malfunction, and we consider any period longer than the minimum number of days of zero rainfall in the GPM time series within the DHM gauge timeseries to be a reporting error and replace those periods with NaN. In doing so, we splice the timeseries into one or more continuous timeframes. The longest period of continuous rainfall over the summer monsoon is the timeseries that we use for analysis, with the caveat that if this time window is less than 50% of the four-month monsoon season (June-September), we exclude that dataset from our analysis. During any given year, we use precipitation data from a minimum of 35 out of 46 rain gauge stations.

GPM IMERG data details

NASA's gridded 30-minute, 0.1x0.1 degree Integrated Multi-satllitE Retrieval (IMERG) product for the Global Precipitation Mission (GPM) is a precipitation product available in *.tif file format from the NASA Precipitation Processing System (PPS) website for public use and research (https://storm.pps.eosdis.nasa.gov/storm/). The product gives global precipitation estimates every 30-minutes in mm/hr from merged and intercalibrated microwave precipitation and microwave-calibrated infrared (IR) estimates. The final product is corrected, and standard error estimates computed with precipitation gauges (Huffman et al., 2019). We use the GPM IMERG 3B V06 Final run 30-minute

surface precipitation product in *.tif format and extract the precipitation timeseries for each grid cell that hosts a DHM rain gauge. We use the standard threshold of 0.1 mm/30-minutes (or 0.2 mm/hr) as the sensitivity limit of the IMERG data and assign all rainfall recorded as <0.1 mm as 0 mm of rainfall.

ICIMOD Kyanjin rain gauge station in Langtang Valley, Nepal

In addition to the DHM network, we use precipitation data from the Kyanjin rain gauge station installed, monitored and maintained by the International Centre for Integrated Mountain Development (ICIMOD) in collaboration with the DHM, located in Langtang National Park. This data is available for research use on ICIMOD's website (http://rds.icimod.org/Home/DataDetail?metadataId=22464&searchlist=True). The Kyanjin station records 10-minute precipitation aggregated into reported hourly totals (mm). It is an automatic tipping bucket gauge with uncertainties of +/- 0.05 mm for total amount and +/- 6 mm/hr for rainfall intensities (see ICIMOD Kyanjin station Metadata Catalog pdf).

We use the data from Kyanjin station because we prefer to have precipitation data from a rain gauge network that spans the length of the Melamchi Valley. The DHM does not report precipitation data for years 2010-2018 in the Langtang Valley, and without a station located in that region, our along-strike analysis of orographic precipitation along the Himalayas is poorly constrained north of the Melamchi Valley and relies on data pulled from stations located in the northwest Trisuli river basin (see main text, Figure 1). We use the Kyanjin station precipitation data to fill this spatial gap in the DHM rain gauge network.

Scaling the IMERG data

In the final run IMERG product, NASA corrects the 30-minute satellite data with monthly rain gauge records by multiplying a difference factor between total satellite precipitation and total rain gauge precipitation (Huffman et al., 2019). We adopt the same approach but on the daily scale. In the process of merging the DHM gauge and the IMERG data, there are periods of time when the rain gauge in question reads rainfall > 0 mm on any given day, but the GPM data reads 0 mm per day. In this instance, scaling the GPM data to match the gauge total results in a missing value; in this case, we treat the DHM rain gauge data as the "ground truth" framework but only use the available rainfall record of IMERG. These small instances of missing values account for up to 10% of the total rainfall during the monsoon season at any given station and result in a discontinuous time series. For the purposes of this analysis, we replace those missing values with zeroes to maintain a continuous time series and accept the source of error in identifying continuous storm periods. We also recognize that we potentially underestimate total monsoon rainfall by up to 26% in the most extreme cases and 5% on average (see Table S1).

In summary, several sources of error are present in our precipitation dataset: (1) gaps in time of no reported data from the DHM gauges (ranges from the odd day to months), (2) suspiciously long periods of zero rainfall recorded by the DHM gauge, (3) by scaling the GPM data, we are left with a few days of NaN that we replace with zero rainfall and finally, (4) we crop incomplete time series so that we are handling the longest continuous series of rainfall and in doing so, ignore large portions of our precipitation dataset and risk losing information or biasing our final results with a smaller sample size. We attempt to rectify this by only using stations with at least 50% of the monsoon timeseries available.

Appendix B. Clustering analysis and PCA

The optimal number of clusters for our dataset is chosen using the "elbow criterion" derived from the common Elbow Method, which looks at the variance explained as a function of the number of clusters. The optimal number of clusters is shown by an "elbow" or discontinuity in slope shown in Figure S6, where variance explained is no longer improved with additional clusters. Here, we use 10 clusters based on the elbow criterion. Most extreme storm events during the summer monsoon fall into similar intensity-duration space ranging from ~5-15 mm/hr and 30 minutes-10-hr durations, but the most extreme events

are outliers in terms of both intensity and duration, especially when considered in principal components space (see Figure S7). To account for these outliers and reduce scatter in each individual cluster, we use 10 clusters (Figure S7), which each include 1-40 ERE's. We then look at the distribution of cluster numbers at each rain gauge station over 2010-2018 and assign a dominant cluster number to the station based on the cluster (i.e., cluster 1, cluster 2, …cluster 10) that includes the majority of EREs registered at that station. This results in the dominant two clusters presented in the main text. However, the exact results vary with each iteration of clustering, and several stations at the transition from cluster A to cluster B fall into one or the other depending on the iteration. We attribute this to the complexity and variability of storms at the "transition zone" between two distinct regimes of rainfall. Our results do not change with analysis of 3-9 clusters.

Appendix C. Landslide catalog and mapping protocol

Our monsoon-driven landslide catalog encompasses landslides that happened during the monsoon (June-September) between years 2010-2014. We intentionally limit our record to before 2015 to eliminate the legacy effects of the April 2015 Mw7.8 Gorkha earthquake. Landslides were hand-mapped by comparing pre- and post-monsoon high resolution photographs (Digital Globe Worldview-2 and -3 satellite imagery). The resolution of the imagery is on the order of 20-50 cm, allowing us to identify and map small landslides and debris flows with minimal scars and runout areas. Adjacent scar areas were mapped as separate landslides to avoid skewness introduced by amalgamation. Over higher elevation, cloud cover, lack of vegetation and glacially sculpted topography limited our ability to accurately map landslides.

We compare landsliding to patterns in precipitation in 2D using a swath profile of landslide density. Landslide density is calculated as the total area of landslides (source and runout) divided by the total area of the inquiry zone in m^2/km^2. The "inquiry zone" is defined as 1-km wide bands running parallel to the range front (see main text Figure 1 for the swath boundary). The curve shown in main text Figure 3 is a 5-km moving average of the binned densities. We combine all landslides from 2010-2014 into the same analysis to look at bulk density of monsoon-driven landsliding and to increase our sample size for signal strength.

Tables

Station	% total monsoon rainfall lost to scaling	% complete monsoon timeseries (avg. 2010-2018)	IAT (hrs)
Bahrabise	8.6	81.8	2.8
Bahunipati	8.2	90.6	4.3
Bhaktapur	4.6	94.1	6.3
Changu Narayan	6.8	91.9	4.5
Chapa Gaun	3.9	96.8	6.8
Chautara	4.6	60.1	3.7
Chisapani Gadhi	4.0	98.9	4.5
Daman	5.6	37.0	5.6
Dhap	10.0	86.6	3.4
Dhulikhel	4.5	82.5	6.4
Dhunche	6.6	80.4	3.5
Dhunibesi	2.8	96.4	5.3
Dolal Ghat	2.3	84.1	7.0
Duwachaur	6.1	72.6	4.9
Godavari	2.1	91.9	4.9
Gumthang	12.8	80.8	3.0
Jitpurphedhi	3.3	91.7	4.1
Kakani	5.1	100	2.7
Kathmandu Airport	4.2	99.3	5.1
Khokana	3.0	99.3	7.1
Khumaltar	4.2	97.6	7.2
Kyangjin	7.2	33.3	12.8
Lele	4.0	93.0	5.0
Mandan	10.8	66.7	8.3
Markhu Gaun	2.7	74.7	6.6
Nagarjun	4.0	86.7	4.0
Nagarkot	4.1	95.4	4.4
Naikap	4.8	69.6	6.2
Nangkhel	3.5	98.5	5.9
Nawalpur	5.2	87.7	2.9
Nuwakot	5.2	88.2	4.1
Panchkhal	4.4	65.1	8.5
Panipokhari	5.0	92.3	4.8
Pansayakhola	8.3	87.3	2.6
Sangachok	2.7	85.8	5.4
Sankhu	8.0	78.1	4.3
Sarmathang	6.7	89.5	1.7
Sundarijal(Alapot)	5.3	96.6	3.8
Sundarijal(Mulkharka)	4.2	96.3	3.2
Tarke Ghyang	5.0	94.8	1.9
Thamachit	9.2	86.2	5.7
Thankot	2.5	93.6	5.6
Thokarpa	7.3	84.1	4.1
Tikathali	4.9	87.1	6.7
Timure	8.8	76.0	8.1

Table S1. Missing data statistics and inter accumulation times (IATs) reported as averages over 2010-2018.

Component	***1***	***2***	***3***	***4***	***5***
Storm depth	0.605			0.488	0.628
Storm duration	0.438	0.408	-0.729	-0.292	-0.158
Storm intensity	0.160	-0.678	-0.114	-0.614	0.354
Peak storm intensity	0.369	-0.564	-0.111	0.380	-0.624
Rainfall prior to the storm peak	0.529	0.236	0.664	-0.395	-0.259
Standard deviation	1.600	1.372	0.583	0.384	0.262
Proportion of variance	**0.512**	**0.377**	**0.068**	**0.029**	**0.014**
Cumulative proportion of variance	**0.512**	**0.889**	**0.957**	**0.986**	**1.000**

Table S2. PCA results including the loadings of each variable in each component as well as the standard deviation, proportion of variance and cumulative proportion of variance explained by each component.

Figures

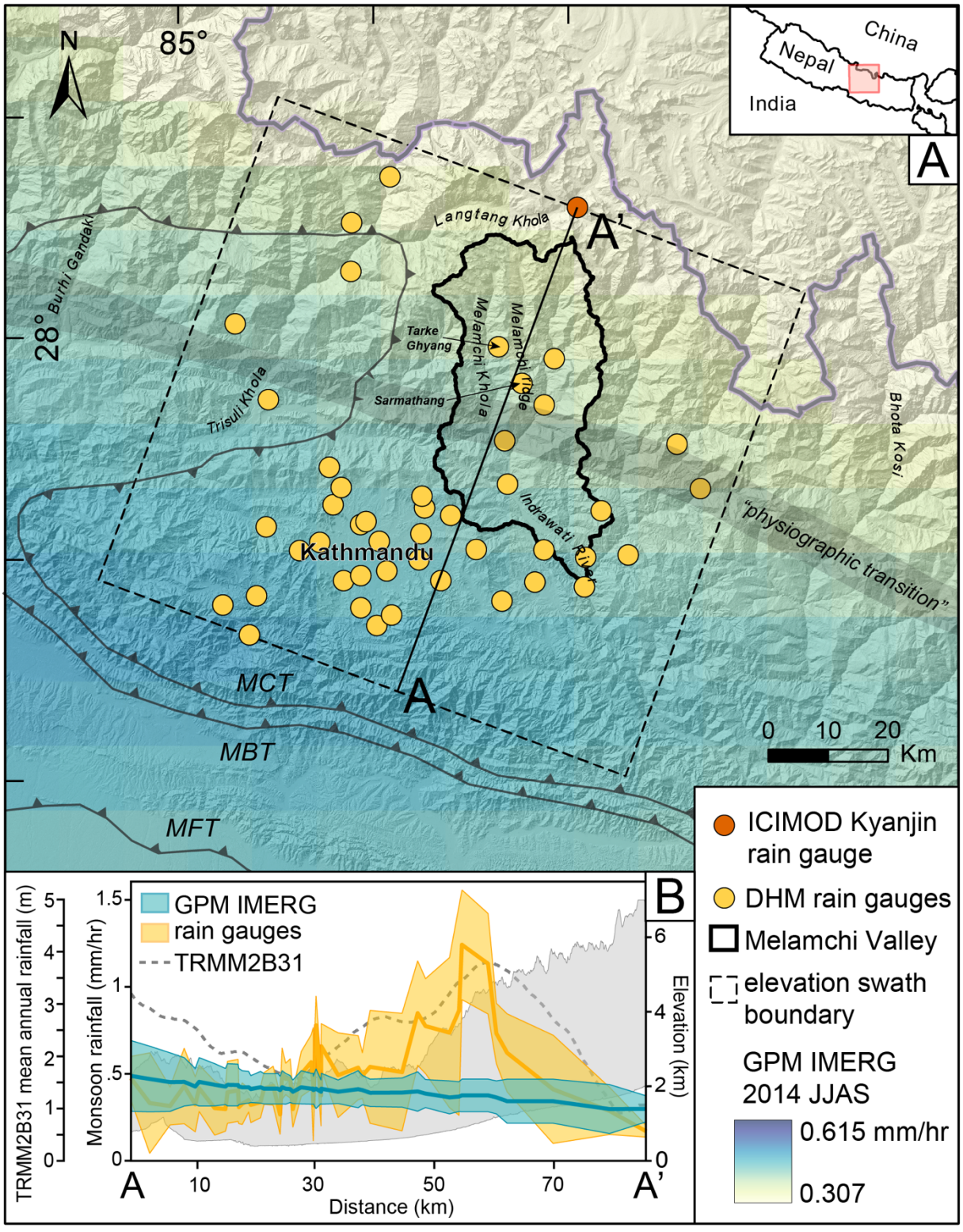

Figure 1. (A) Locations of the Melamchi-Indrawati catchments in central Nepal (inset) and rain gauges

used in this study. The gridded GPM IMERG product is visualized as average rainfall intensity over a single monsoon period (e.g. 2014), and the dashed box indicates the bounds of the elevation swath profile shown in (B). The dark grey "physiographic transition" is a prominent change in topography, relief, precipitation, and channel gradient (Wobus et al., 2003, 2006). **(B) NNE** profile of average monsoon intensity (calculated as total rainfall volume over the monsoon period) measured by the rain gauge network and GPM IMERG data from 2010-2018 and with 95% confidence bounds. The peak in monsoon rain gauge data at ~55 km is similarly located to the peak in rainfall derived from long-term satellite records from TRMM2B31 data (Bookhagen and Burbank, 2006).

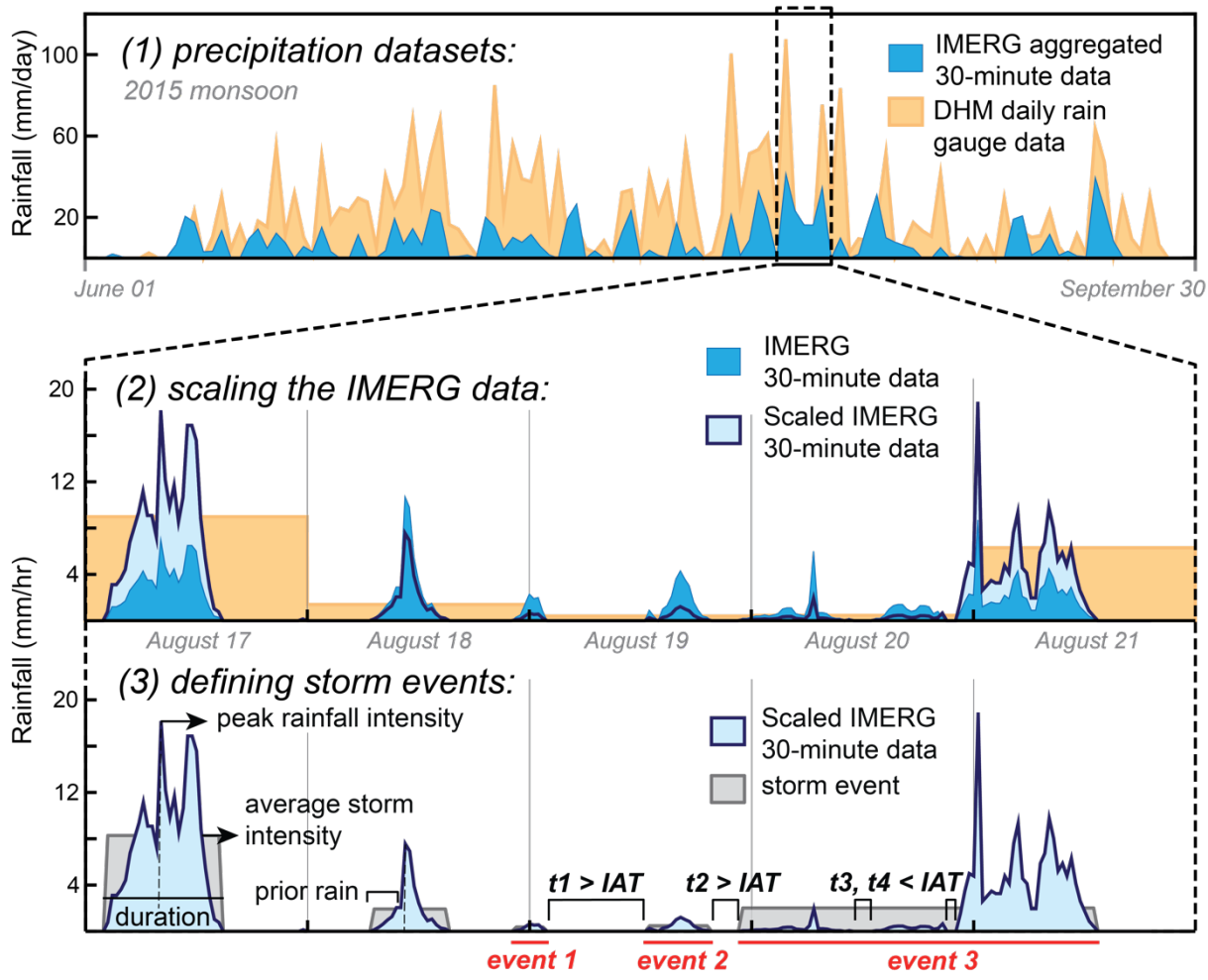

Figure 2. Process of calibrating the IMERG data based on the rain gauge record (2) and defining storm periods (3) using inter-accumulation times. Storm periods integrate across dry periods of time < IAT (i.e., t3, t4). Five characteristics describe each storm event: average storm intensity, peak storm intensity, duration, depth, and prior rain to the storm peak.

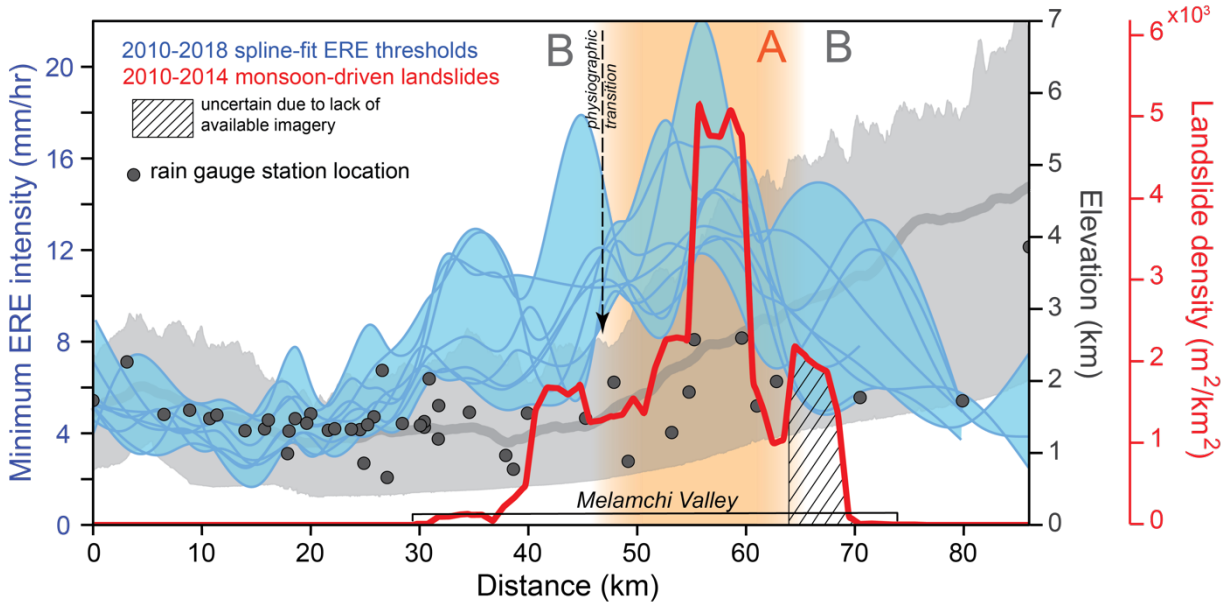

Figure 3. Profile across the central Nepal Himalaya (A-A' from Figure 1) showing orographic relationships between elevation, extreme rainfall event (ERE) intensity thresholds and landslide density. Rain gauge station locations are plotted with respect to elevation derived from a 30 m DEM. Landslides were mapped within the Melamchi watershed during the period of 2010-2014, prior to the 2015 Mw7.8 Gorkha earthquake, and are potentially undercounted north of ~64 km due to unavailable imagery and/or cloud cover. The two primary clusters A and B are shown in orange and gray, respectively. ERE thresholds at each rain gauge station are fit with a smoothing spline interpolation for each monsoon year (2010-2018) shown in blue. Cluster A (orange) is collocated over the highest ERE thresholds and a peak in monsoon-driven landsliding (red). The approximate location of the physiographic transition (Wobus et al., 2006) coincides with the southern boundary of cluster A.

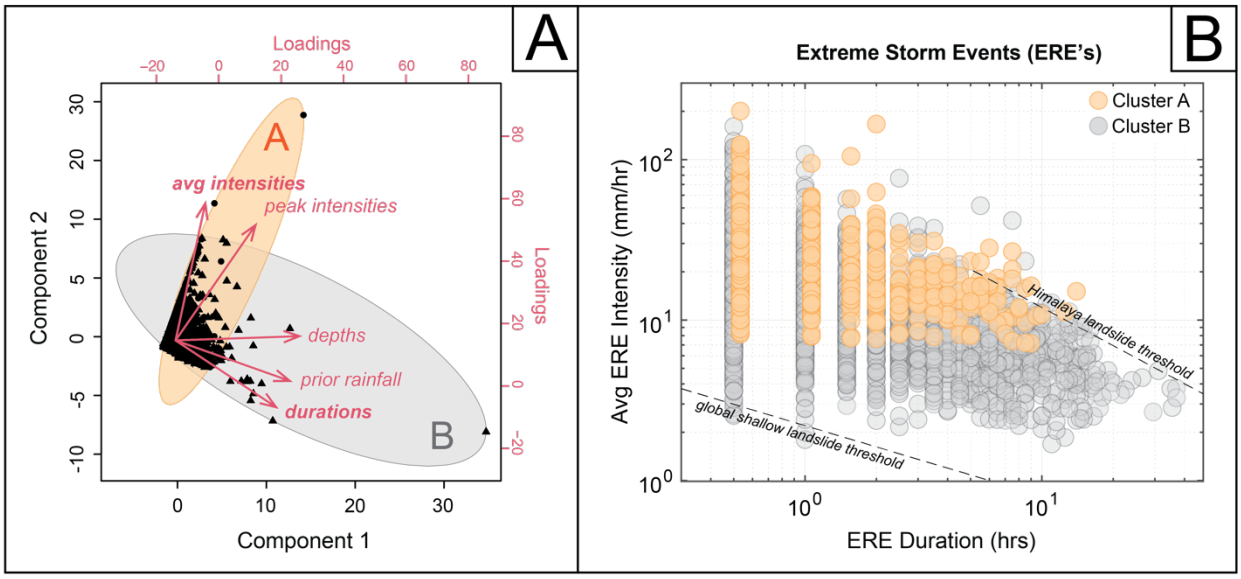

Figure 4. (A) Principal components analysis (PCA) biplot with variables axes shown in red and clusters A and B shown in orange and gray, respectively. The same color scheme is used in (B), where individual EREs are plotted with respect to the duration and average intensity of each event. A global landslide threshold (Guzzetti et al., 2008) and a Himalaya-specific landslide threshold (Dahal & Hasegawa, 2008) are also plotted. A small number of storms fall above the Himalaya-specific threshold.

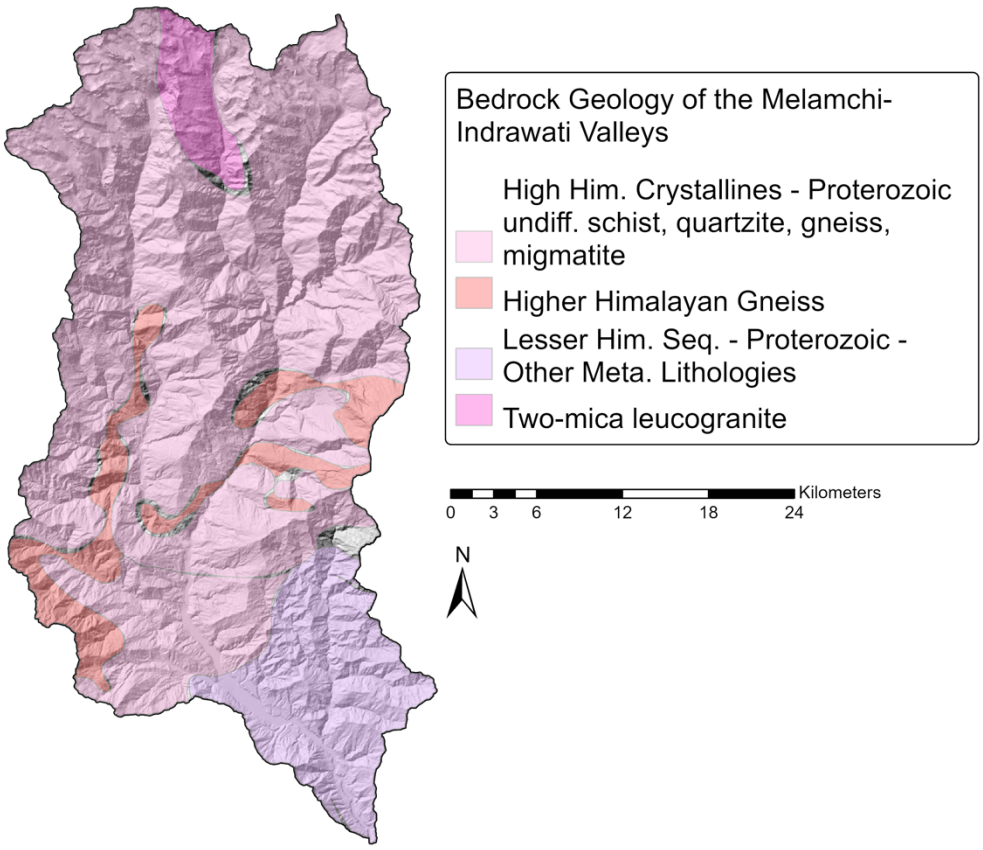

Figure S1. Bedrock geology of the Melamchi-Indrawati Valleys, central Nepal (Dhital, 2015), which is almost exclusively the Higher Himalayan crystalline sequence of gneiss and migmatite.

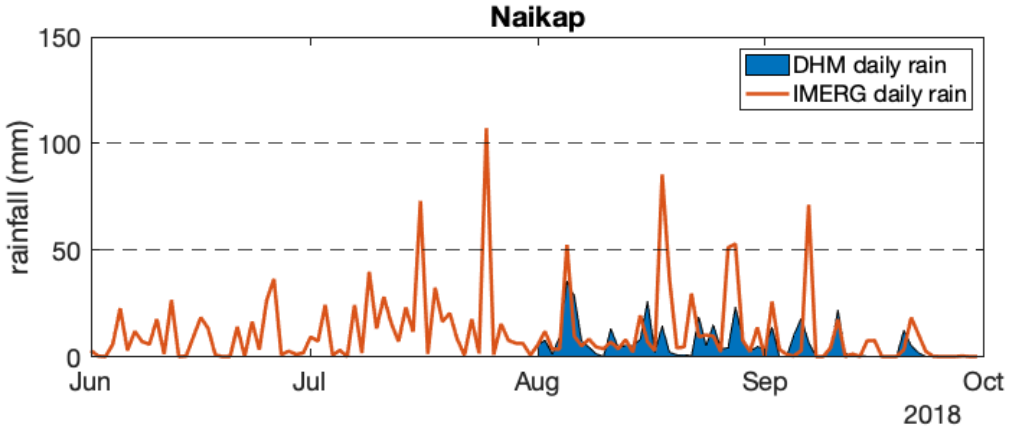

Figure S2. Example daily timeseries from station Naikap showing both the DHM rain gauge data (blue) and the summed 30-minute IMERG data (orange). In this instance, rain gauge data exists for August-September (50% of the monsoon), and so this station was not included in the 2018 analysis because the sample size of storms is too small to adequately define a 90th percentile and EREs. Also note that on most days, the IMERG data overestimates rainfall at this station, which is located south of the Melamchi Valley near Kathmandu.

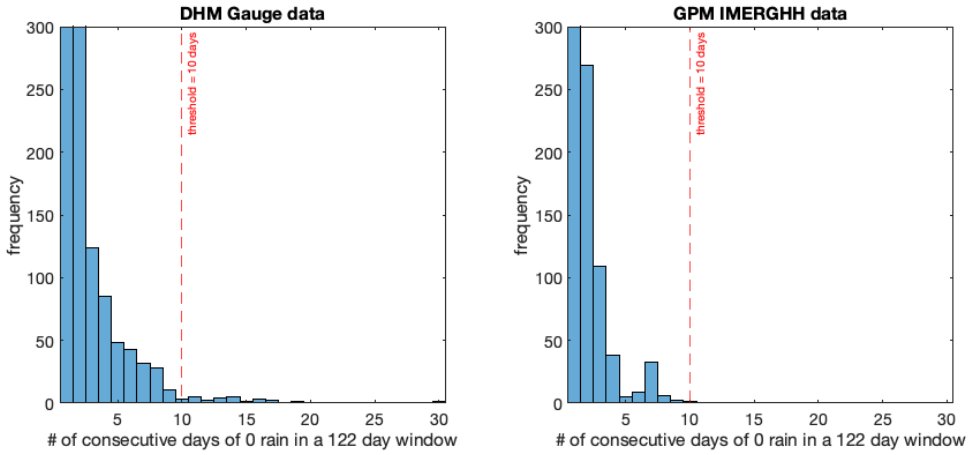

Figure S3. Frequency distribution histograms of periods of consecutive days of 0-rainfall, where the x axis is the number of consecutive days, and the y axis is the frequency of those periods (for every station in our dataset for the year 2018). The dashed red line indicates the maximum dry period in the IMERG data (here, 10 days). We apply this threshold to the gauge data to eliminate periods where rain gauges recorded 0 rainfall but were likely not working during that time.

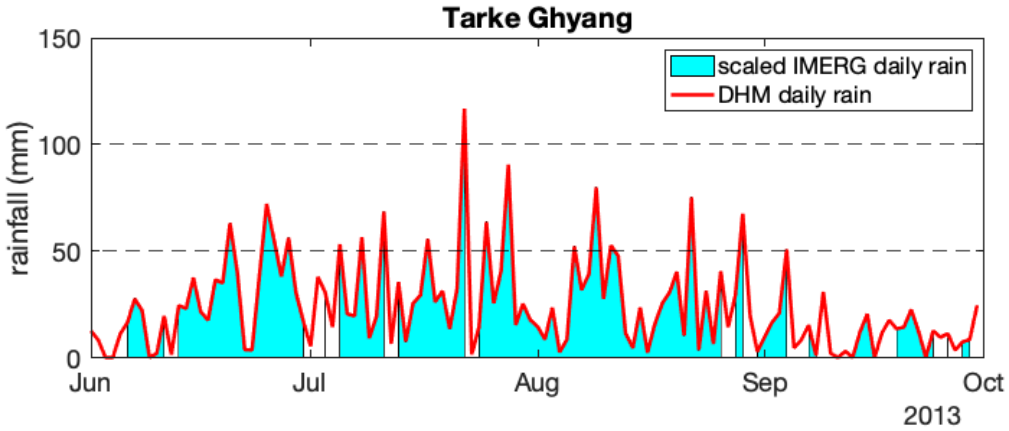

Figure S4. Example daily timeseries at station Tarke Ghyang with DHM rain gauge data (red) and scaled IMERG data (cyan). Note the unfilled days where the IMERG data read 0-rainfall (and therefore could not be scaled). We only use IMERG data when it is available, and so these periods are considered 0 rainfall and account for a 1.67% underestimation of gauge rainfall (mm) for this monsoon year and at this station.

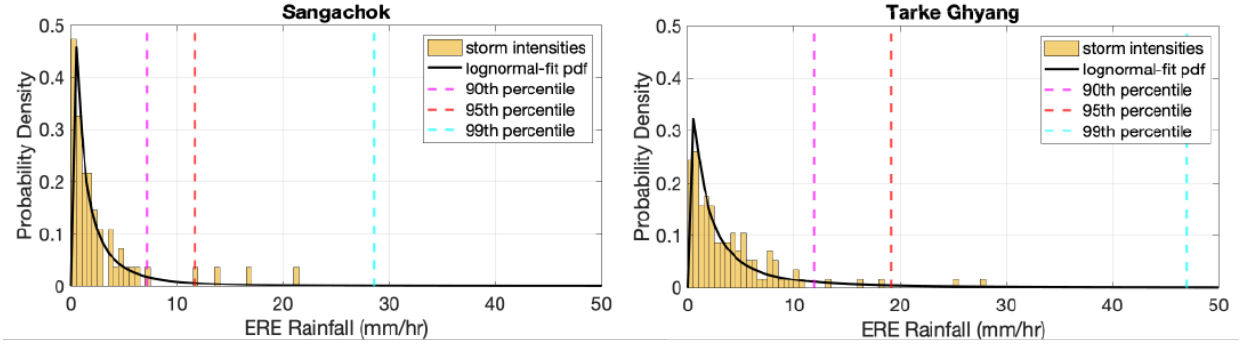

Figure S5. Example distributions of storms at stations Tarke Ghyang and Sangachok, where storms are binned with respect to average intensity (mm/hr). We fit a lognormal pdf to the storm distributions and define any storm that falls above the 90th percentile (pink dashed line) as an extreme rainfall event (ERE).

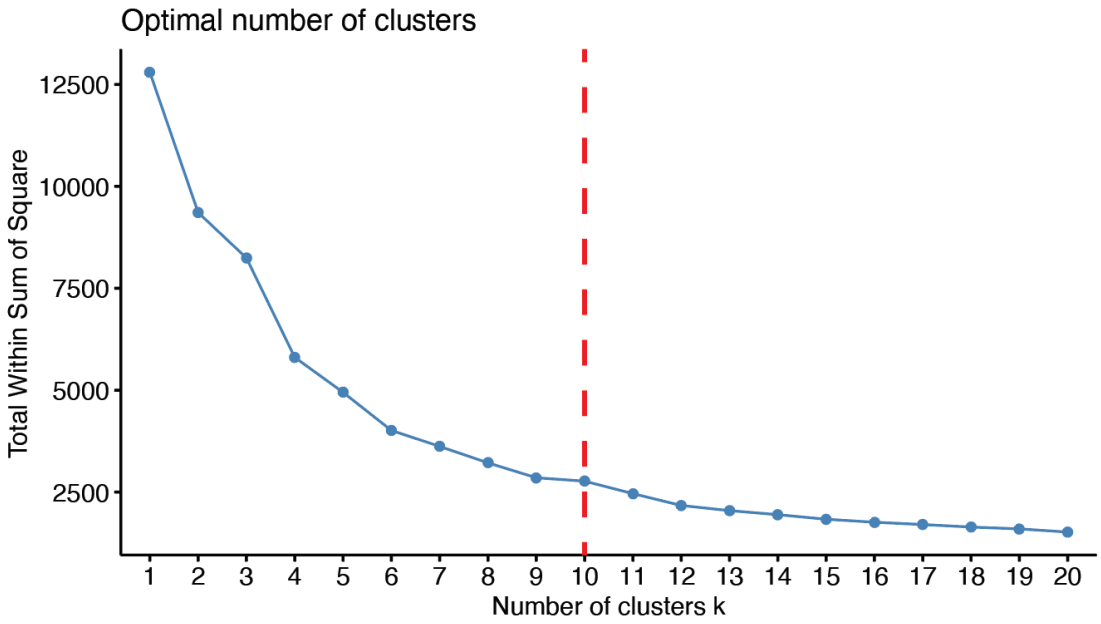

Figure S6. Elbow analysis determining the appropriate number of clusters for our dataset (10).

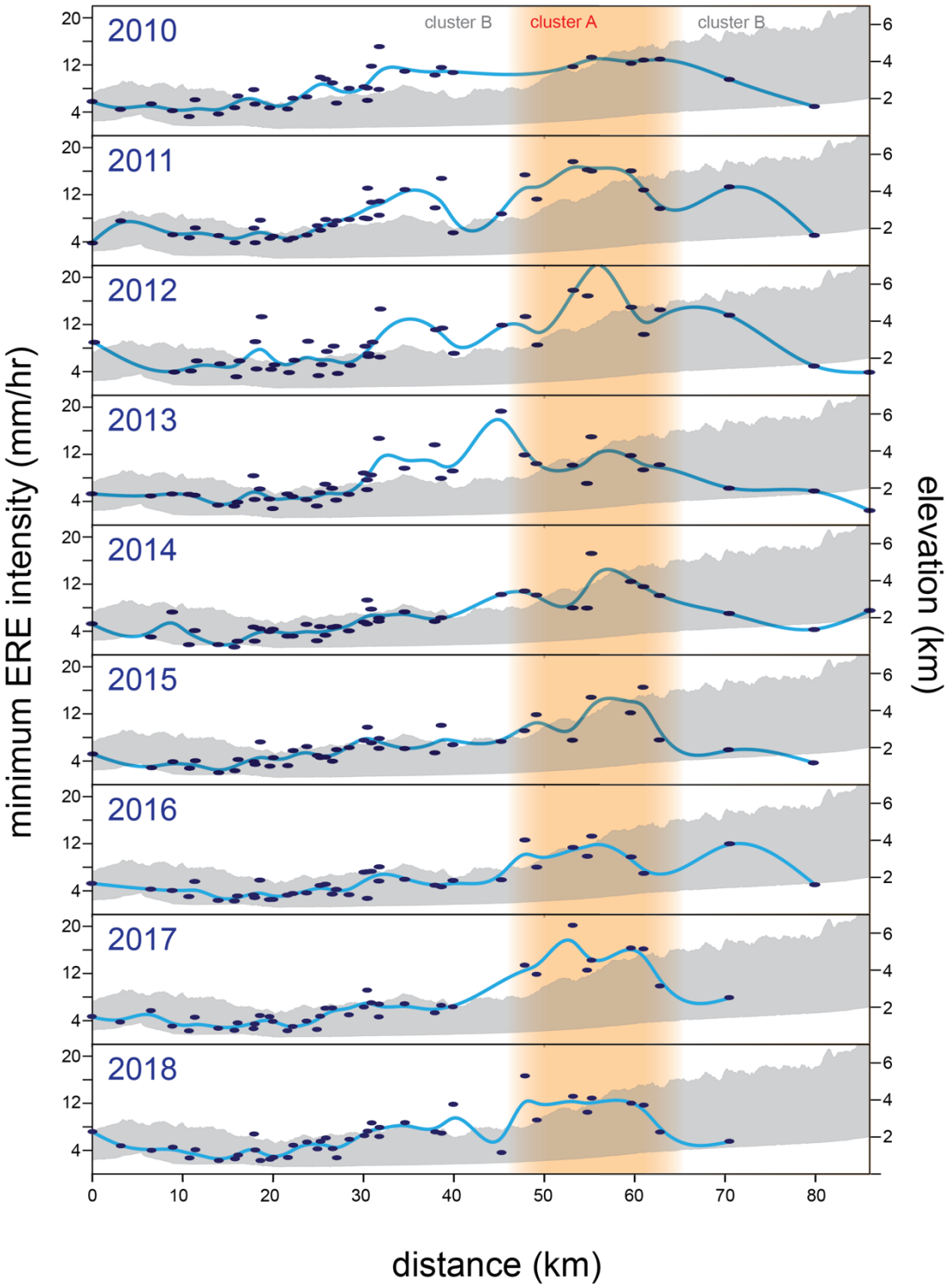

Figure S7. Profile figure of topography, threshold ERE rainfall and spatial distribution of clusters A and B (same as Figure 3, main text) for each year of our analysis (2010-2018). Here we show the ERE thresholds defined at each gauge (dark blue dots) for each year to demonstrate that our smoothing spline interpolations (blue lines) fit the threshold data well.

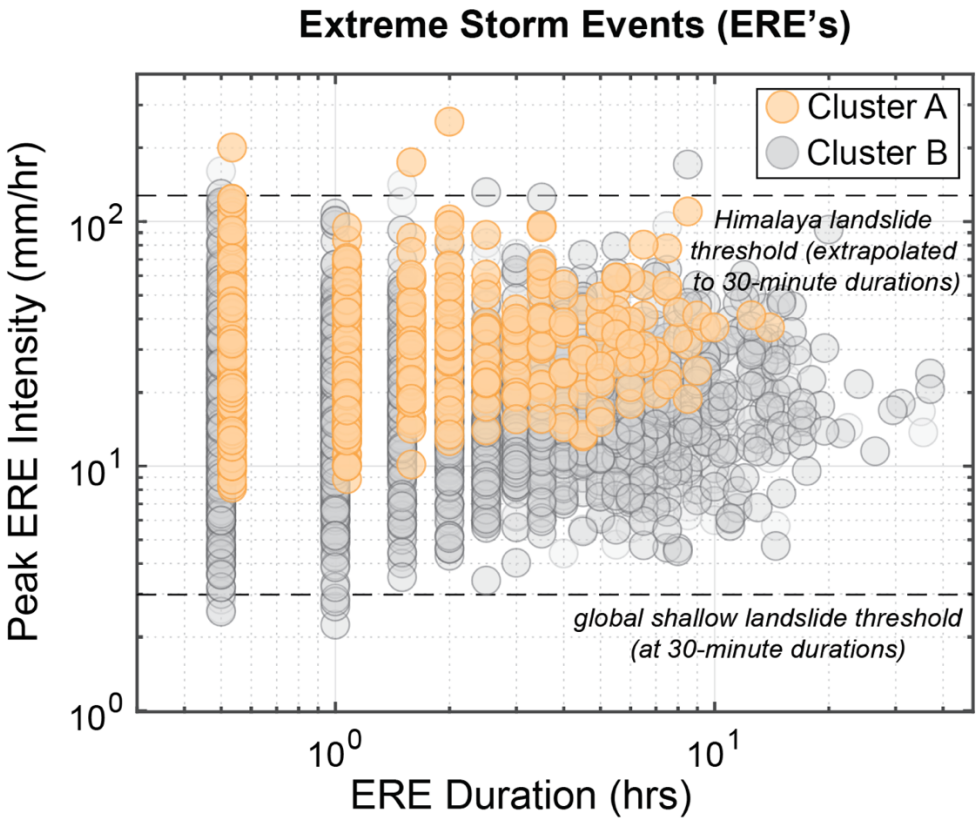

Figure S8. Intensity-duration plot of all 2010-2018 EREs, plotted with respect to the peak 30-minute intensity of the storm event over its duration. Landslide thresholds are plotted at 30-minute intensity (from Dahal and Hasegawa, 2008; Guzzetti et al., 2008).

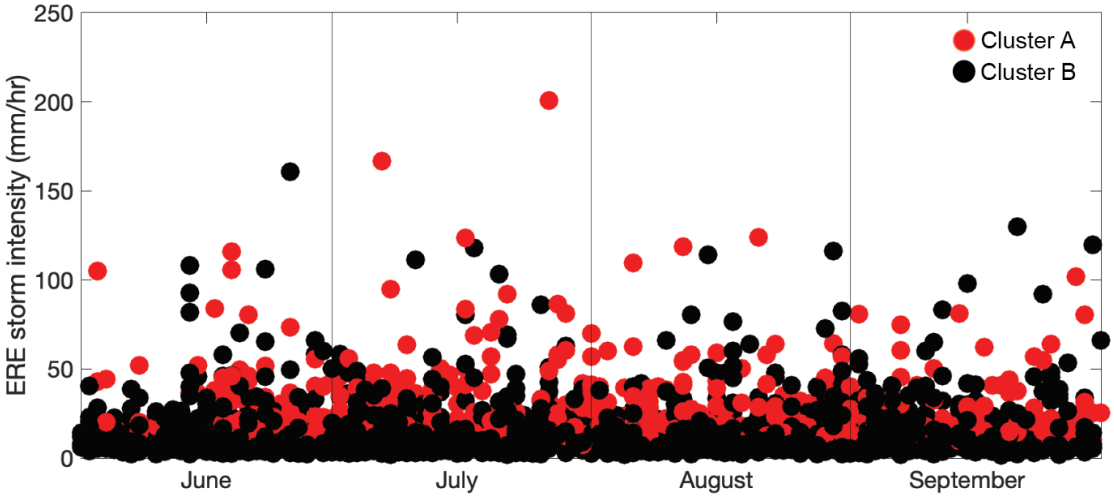

Figure S9. EREs plotted with respect to timing in the monsoon season, colored by cluster. We observe no correlation with cluster and timing; EREs in either cluster are likely to occur at any point during the monsoon season.